Acoustic signals associated with vortexline reconnection
in oblique collision of two vortex rings

Shizuko Adachi　(安達静子)　Institute of Computational Fluid Dynamics

Katsuya Ishii　(石井克哉)　Department of Applied Physics, Nagoya University

Tsutomu Kambe (神部　勉)　Department of Physics, University of Tokyo

Abstract: A theory of vortex sound formulated in the form of multipole expansions is applied to the oblique collision of two vortex rings at right angles. Using the theoretical formula for the far-field acoustic pressure excited by a time-dependent localized vorticity distribution, the coefficients of the multipole modes of the wave pressure are estimated by the numerical data of computer simulation. Time evolution of the vorticity field is obtained by solving a viscous incompressible vorticity equation with a vorticity-potential method developed for a three-dimensional vorticity field in a bounded domain. Numerical simulations are carried out for two kinds of vortex rings with the same core parameters but different ring radii, and the details of the vortex motion during the oblique collision are studied numerically. Computed main-mode amplitudes of the wave pressure excited by the vortex motion are found to be consistent with those of the experimentally observed acoustic wave not only qualitatively but also quantitatively unlike the previous study. From comparison of the quadrupole and octapole modes of the far-field acoustic pressure between the computation and the experiment, it is possible to estimate the slenderness ratio of a core radius to a ring radius of the experimental vortex ring. It is remarkable that the present simulation gives data identifying the source region for the wave emission, and that a characteristic evolutionary pattern of the vortex motion is responsible for the observed up-down asymmetry of the radiation. Strong acoustic source is identified at the location where vortexline reconnection occurs.

I. INTRODUCTION

The theory of vortex sound is developed successfully to describe the acoustic waves driven by unsteady fluid motion with localized vorticity field at low Mach numbers and high Reynolds numbers. Based on mathematical formulation in the form of multipole expansions, explicit formulae of the wave profile are given in terms of the time-dependent vorticity field. Under the condition that a typical Mach number M is much less than unity, the whole field is separated into two fields: inner flow and outer wave regions. Far-field expression of the acoustic pressure is obtained by matching of the two solutions of the inner flow region and the outer wave region in an intermediate region. We present a review of the new general mathematical formulation for the vortex sound [1-4] in Sec. II.

Kambe *et al.*[4] compared the results from a laboratory experiment and a computer simulation for an oblique collision of two vortex rings at right angles. While the normalized mode coefficients from the computer simulation succeeded in reproducing the qualitative feature of the experiment, they pointed out a quantitative discrepancy as follows. The dimensionless quadrupole mode amplitudes from the simulation are by 25 times smaller than the experiment and the octapole mode amplitudes by 125 times smaller. They argued that this discrepancy resulted from the Reynolds number in the simulation which is much smaller than the experimental number. However there is another point to be examined critically that they used vortex rings which are not thin even at the initial setup and those vortex rings become too thick in the collision stage compared with the experimental vortex rings. The point is that the large slenderness ratio may consequently be the reason of the discrepancy. In the present paper we therefore examine the effect of the slenderness ratio on the mode coefficients. Two kinds of vortex rings with the slenderness ratio $\lambda_0 = 0.2$ and 0.1 are chosen for the investigation.

The vorticity-potential method [5,6] for solving a viscous incompressible vorticity equation is reviewed in Sec. III. With a time-dependent vorticity distribution and a vector potential obtained by this method the quadrupole and octapole mode amplitudes are eval-

uated.

Computational results of the vortex motion and acoustic mode amplitudes are presented in Sec. IV. From comparison with the experiment we estimate a slenderness ratio of the experimental vortex rings. In order to clarify which parts of the region in space contribute to the dominant mode amplitudes we present the spatial distribution of the third and the fourth order time derivatives of the impulse density of vorticity at the instance when those amplitudes reach the maximum or the minimum. We focus on the vortex motion which is characteristic to the oblique collision and results in the excitation of asymmetric acoustic waves. The location of the vortexline reconnection is shown to coincide with the strong source region for the acoustic emission. Concluding remarks are given in Sec. V.

II. VORTEX SOUND FORMULATION

Neglecting the terms of $O(M^2)$, the basic equation in the inner region reduces to the incompressible Navier-Stokes equation. In the outer region the adiabatic relation $p - p_0 = c^2(\rho - \rho_0)$ is satisfied approximately. Neglecting the term of $O(Re^{-1}M^2)$ with the Reynolds number of the inner source flow Re which is assumed to be much larger than unity, we obtain the wave equation for the pressure p. Matching the outer solution to the inner solution is carried out in an intermediate region. The details of the procedure is presented in Ref.[4].

In the case of unbounded space where there is neither a solid body nor an external force, the far-field expression retaining only the terms of $O(r^{-1})$ for sufficiently large $r = |\mathbf{x}|$ is

$$p^{(f)}(\mathbf{x}, t) = -\rho_0 P_0^{(1)}(t_r)\frac{1}{r} - \frac{\rho_0}{c^2}Q_{ij}^{(3)}(t_r)\frac{x_i x_j}{r^3} + \frac{\rho_0}{c^3}Q_{ijk}^{(4)}(t_r)\frac{x_i x_j x_k}{r^4} + \cdots \tag{1}$$

where superscript (n) denotes the n-th time derivative and $t_r = t - r/c$ the retarded time. The coefficients Q's are

$$Q_{ij}(t) = -\frac{1}{12\pi}\int (\mathbf{y} \times \omega)_i y_j d^3y \quad , \quad Q_{ijk}(t) = \frac{1}{32\pi}\int (\mathbf{y} \times \omega)_i y_j y_k d^3y, \tag{2}$$

where ω is obtained by solving the vorticity equation in the inner region. The first isotropic term in (1) is related to the rate of energy dissipation as

$$P_0(t) = -\frac{5-3\gamma}{12\pi}\frac{1}{c^2}K^{(1)}(t) , \qquad K(t) = \frac{1}{2}\int v^2(\mathbf{y},t)d^3y, \tag{3}$$

where K is the total kinetic energy and γ is the ratio of specific heats ($\gamma = 7/5$ for the air).

In this paper we study the oblique collision of two vortex rings at right angles. The geometry of the initial set up of the experiment by Kambe *et al.* is reproduced in Fig.1 from [4]. The centers of vortex rings are located on the (x_2, x_3) plane with $\theta = \pi/2$. Both vortex rings move in the direction towards the origin. The expression of the pressure observed at a far point (r_{obs}, θ, ϕ), satisfying the symmetry, is expressed as

$$p(\theta, \phi, t) = A_0(t) + A_1(t)P_2^0(cos\theta) + A_2(t)P_2^2(cos\theta)cos(2\phi)$$
$$+ B_1(t)P_3^0(cos\theta) + B_2(t)P_3^2(cos\theta)cos(2\phi) + \cdots, \tag{4}$$

where $P_n^k(cos\theta)$ is the Legendre polynomial of the n-th order ($k = 1, \ldots, n$). The coefficients in the above expression are given by

$$A_0 = -\frac{\rho_0}{r_{obs}}P_0^{(1)} , \quad A_1 = -\frac{\rho_0}{c^2 r_{obs}}Q_{33}^{(3)} , \quad A_2 = -\frac{\rho_0}{6c^2 r_{obs}}[Q_{11}^{(3)} - Q_{22}^{(3)}], \tag{5}$$

$$B_1 = \frac{\rho_0}{c^3 r_{obs}}[Q_{333}^{(4)} - (1/5)Q_{3kk}^{(4)}] , \quad B_2 = \frac{\rho_0}{c^3 r_{obs}}\frac{1}{30}[\tilde{Q}_{113}^{(4)} - \tilde{Q}_{223}^{(4)}], \tag{6}$$

where the tilde symbol denotes $\tilde{Q}_{113} = Q_{113} + Q_{131} + Q_{311}$. With using the tensors

$$F_{ij} = \int y_i N_j d^3y = \int (v_j v_i - \frac{1}{2}v^2\delta_{ji})d^3y, \tag{7}$$

$$G_{ijk} = \int y_i y_j N_k d^3y , \quad \mathbf{N} = \mathbf{v} \times \omega, \tag{8}$$

the order of the time derivative in the expression of the mode amplitudes is reduced by one, and we have

$$A_0 = -\frac{\rho_0}{15\pi c^2 r_{obs}}F_{ii}^{(2)}, \tag{9a}$$

$$A_1 = -\frac{\rho_0}{12\pi c^2 r_{obs}}[F_{11} + F_{22} - 2F_{33}]^{(2)}, \tag{9b}$$

$$A_2 = \frac{\rho_0}{24\pi c^2 r_{obs}}[F_{11} - F_{22}]^{(2)}, \tag{9c}$$

$$B_1 = \frac{\rho_0}{40\pi c^3 r_{obs}}[-2G_{311} - 2G_{322} + 2G_{333} - G_{113} - G_{223}]^{(3)}, \tag{9d}$$

$$B_2 = \frac{\rho_0}{240\pi c^3 r_{obs}}[2G_{311} - 2G_{322} + G_{113} - G_{223}]^{(3)}. \tag{9e}$$

We use these expressions in the present calculation.

III. VORTEX COLLISION SIMULATION

In order to obtain the mode coefficients A and B of the the far-field pressure in (4), the vorticity ω in the inner region should be evaluated. The governing equations for the vorticity ω and the induced velocity $\mathbf{v}$ are given by

$$\partial_t \omega - \nabla \times (\mathbf{v} \times \omega) = \nu \nabla^2 \omega, \tag{10}$$

$$\nabla \cdot \mathbf{v} = 0 \tag{11}$$

Introducing a vector potential $\mathbf{A}$ by $\mathbf{v} = \nabla \times \mathbf{A}$ together with the solenoidal condition $\nabla \cdot \mathbf{A} = 0$, the vector potential $\mathbf{A}$ satisfies the Poisson equation $\nabla^2 \mathbf{A} = -\omega$. The solution is given exactly by the Poisson integral

$$\mathbf{A}(\mathbf{x}, t) = \frac{1}{4\pi} \int \frac{\omega(\mathbf{y}, t)}{|\mathbf{x} - \mathbf{y}|} d^3 \mathbf{y}. \tag{12}$$

The vorticity-potential method [5,6] developed for a three-dimensional bounded vorticity field is used in the present numerical simulation. When the vorticity distribution is given at one time step, the vector potential (12) is evaluated at grid points on the boundary surface of the computational domain. Since ω is localized, the contribution of integrand to the Poisson integral is confined in the localized region and ω can be assumed to be zero on the computational boundary during the simulation. Then the Poisson equation with these boundary data is solved using the SOR method in order to obtain the values of the vector potential on grid points in the interior domain. We use the second order central difference scheme in space. Time marching to the next step following (10) is carried out with the fourth order Runge-Kutta-Gill method using the vorticity and the vector potential obtained above. In the present simulation, the number of operations is reduced as follows. The evaluation of the Poisson integral is carried out for coarse grid points on the boundary surface, then they are interpolated with a surface cubic Spline method to give the boundary values on fine grid points. The whole integration domain in the *r.h.s.* of (12) is divided into subdomains. Since the distance between boundary points and the vorticity field is large, the factor $1/|\mathbf{x} - \mathbf{y}|$

can be expressed by a power series in $r^i = | \mathbf{x} - \mathbf{y}_c^i |$ which is the distance between the boundary point $\mathbf{x}$ and the center of the i-th subdomain of the integration $\mathbf{y}_c^i$, and we take the first order term of the expansion. Then the integration only on ω is evaluated for each subdomain.

Initially two vortex rings are set to collide at right angles. The vortex ring radius is R and the core radius is a. The vortex ring has a Gaussian vorticity distribution in the core. In order to examine the effect of slenderness ratio $\lambda_0 = a_0/R_0$ we choose two sets of parameters. Both sets have the same vortex core parameters $\Gamma = 20\pi$ (circulation), $a_0 = 1.0$ and kinetic viscosity $\nu = 0.1$, but different vortex ring radii $R_0 = 5.0, 10.0$.

During the numerical simulation we checked the conservation property of the vorticity distribution which is to be satisfied by motion of the incompressible fluid in unbounded region.

IV. RESULTS AND DISCUSSION

Side view(from the x_1 axis) and top view(from the x_3 axis) of the collision of two vortex rings at right angles for the two sets of parameters are presented in Fig.2. The isovorticity surface of magnitude with 40% of the maximum at each instance is illustrated. Two vortex rings appear to be translated with mostly constant speed except for the interacting parts. The vortex cores come in contact with each other at about $t \simeq 1$. The contacting parts are elongated to the positive x_3-direction. As the contacting parts become large, the rings are stretched in the x_1-direction, which is due to the reconnection phenomena of vortex lines. Finally the vorticity of the contact parts is diminished and two vortex rings become one vortex ring.

If a vortex ring is very thin, the stable vorticity distribution in the core is considered to be Gaussian. The translational velocity of the ring without the interaction of other rings is estimated by Saffman's formula [7]

$$U = \frac{\Gamma}{4\pi R}\{\log\frac{8R}{a} - 0.558\}. \tag{13}$$

Here, the core radius a is given by

$$a = \sqrt{4\nu(t_0 + t)} \quad , \quad a_0 = \sqrt{4\nu t_0}. \tag{14}$$

Using the above velocity of the ring, the Reynolds number of the ring motion is estimated to be $Re = UR/\nu$. On the other hand the Reynolds number of the circulation is $Re^* = \Gamma/\nu$. For the motion of one vortex ring several time scales are recognized: the first is the time scale of the translational motion as a whole $T_1 = R/U$, the second is that of the local core deformation $T_2 = a/U$, the third is the period of the core rotation $T_3 = a^2/\kappa$, where $\kappa = \Gamma/2\pi$, the fourth is the viscous life time of the core $T_4 = a^2/(4\nu)$ and the fifth is the life time of the vortex ring as a whole $T_5 = R^2/(4\nu)$. Velocities relating to the above time scales T_1, T_3 and T_4 are $U_1^* = U$, $U_3^* = \kappa/a$ and $U_4^* = \nu/a$ respectively. Parameters of the present simulation including the above time scales are listed in Table I. Those of the numerical simulation and the experiment in Ref.[4] are also presented for comparison.

One of the necessary conditions for the numerical simulation is that a period of the simulation must be much smaller than the life time of the vortex ring T_5. It is also desirable that the interaction in which we are interested should finish before the core radius becomes large. Our calculation meets these conditions.

In order to compare the calculated mode amplitudes with the experiment, we normalize them with the vortex ring radius R_0 and the translational velocity U_0. The normalized amplitudes are

$$\tilde{A}_n = A_n/[\rho_0 R_0 U_0^4/(c^2 r_{obs})] \quad , \quad \tilde{B}_n = B_n/[\rho_0 R_0 U_0^5/(c^3 r_{obs})]. \tag{15}$$

The normalized time is $\tilde{t} = t/(R_0/U_0)$. The calculated mode amplitudes are plotted in Fig.3. The origin of time $\tilde{t}$ is chosen at the time of the positive peak of $\tilde{A}_1$. Since the acoustic waves prior to the interaction were removed in the experimental results, we subtract the amplitudes of non-interacting vortex rings from those of two interacting vortex rings and present the resultant mode amplitudes in Fig.3. The amplitudes are drawn with thick solid lines for $R_0 = 5$ and with thick dashed lines for $R_0 = 10$. The observed amplitudes are shown with thin lines in the same figure for comparison.

In the case of the monopole emission, the mode amplitude is given by the rate of energy dissipation which depends directly on the viscosity. It is noted that the Reynolds numbers in the simulation and in the experiment differ by about 50 times.

For both vortex ring radii $R_0 = 5$ and 10, the calculated mode amplitudes reproduce qualitatively well the experimental amplitudes. While the main mode amplitudes with $R_0 = 10$ coincide with the experimental ones quantitatively, the calculated peak value of $\tilde{A}_1$ and $\tilde{B}_1$ for $R_0 = 5$ is about a half of the experimental value. When we normalized the mode amplitudes presented in Fig.3, we used the translational velocity of the vortex ring estimated with Saffman's formula. The numerical simulation of a single vortex ring shows that the initial translational ring velocity is very close to Saffman's value, but the ring velocity decreases gradually because of the viscous effect. If we took account of this slow-down of the vortex ring before the vortex collision and used a smaller value for the translational velocity in the normalization, the peak values of the mode amplitudes would increase by about 50%. Then the experimental values of $\tilde{A}_1$ and $\tilde{B}_1$ fall in between the calculated values for $R_0 = 5$ and those for $R_0 = 10$. It might be concluded that the experimental slenderness ratio would fall in between the two values used in the simulation. In addition, considering the fact that the vortex cores grow in size during the interaction, we estimate that the slenderness ratio of the experimental vortex ring would be between 0.15 and 0.25.

Since all parameters in the present computer simulation are different from those in Ref.[4], it is not easy to conclude what brings the large difference between these two simulations. But one of the most striking difference seems to be the fact that the life time of the vortex core T_4 and the life time of the vortex ring T_5 (See Table I) are much smaller in Ref.[4] than those in the present calculation. In the numerical simulation of Ref.[4] the vortex rings are not very thin even at the initial state (the slenderness ratio is two or four times of our computation) and they become thick during the collision stage. On the other hand the vortex rings in the present study keep thin even during the collision process. The difference in the time evolution of the vortex ring structure must be one of the most important reason

why these two simulations bring so different magnitude to mode amplitudes.

We next look into the details of the vorticity field related to the amplitudes A_1 and B_1, because the amplitude A_2 is much smaller than A_1 and the amplitude B_2 is negligible compared to B_1 in both the experiment and the simulation. As seen from Eqs.(2),(5) and (6) the amplitudes $A_1(t)$ and $B_1(t)$ depend on the spatial distribution and time evolution of only the third component of the impulse density of the vortex system $\mathbf{p} = \frac{1}{2}\mathbf{y} \times \omega$. The amplitudes $A_1(t)$ and $B_1(t)$ are proportional to the space integral of

$$a_1(\mathbf{y},t) = \frac{2}{12\pi}p_3^{(3)}(\mathbf{y},t)y_3 \quad , \quad b_1(\mathbf{y},t) = \frac{2}{32\pi}p_3^{(4)}(\mathbf{y},t)(y_3^2 - \frac{1}{5}y^2). \tag{16}$$

In order to see such part of the vortex ring which gives significant contribution to the above integrand, we first calculate the spatial distribution of the third and fourth time derivatives of p_3 at the time around the peaks of the amplitudes A_1 and B_1. At the time around the positive peak of the amplitude B_1 (time α), both $p_3^{(3)}$ and $p_3^{(4)}$ have large magnitude in the lower part of the vortex ring. They have large magnitude in the upper-right and upper-left part of the ring at the time around the positive peak of the amplitude A_1 (time b), and then the regions with large magnitude move further left or further right and downward direction at the time around the negative peak of B_1 (time β). This time evolution of the space distribution of $p_3^{(3)}$ and $p_3^{(4)}$ is well understood from that of the vorticity field during the collision. The projective side view(from the x_2 axis) of the isovorticity surface of magnitude with 40% of the maximum is presented in Fig.4(a). The vorticity profile of Fig.4(a) shows that the first collision occurs at the top part of the two vortex rings. Subsequently, the top part stretches upward around the time α. As the collision proceeds the interacting region widens sideward along the cores. In the upper right and left parts, the vorticity field changes very rapidly and those parts stretch in the outward direction of the vortex ring at the time b. Then the total downward motion of the vortex ring pulls down the collision region in the upper part which expands outward around the time β.

We next calculate the integrands a_1 and b_1. The projective side views of the distribution of a_1 and b_1 from the x_2 axis are presented in Figs.4(b) and (c) for the vortex ring with

$R_0 = 10$ at the time α, b and β. The region with large magnitude of a_1 and b_1 is drawn with black. The $x_3 = 0$ line is shown with a thick line on the grid. Since the lower part of the vortex ring locates near the (x_1, x_2) plane, the weighting factor y_3 on $p_3^{(3)}$ or $y_3^2 - \frac{1}{5}y^2$ on $p_3^{(4)}$ reduces the contribution from the lower part but enhances the contribution from the upper part. Therefore the regions with large magnitude of a_1 and b_1 at the time α exist in both the lower and the upper parts. On the other hand the regions with large magnitude of a_1 and b_1 exist only in the upper part at the time b and β because $p_3^{(3)}$ and $p_3^{(4)}$ themselves have large magnitude in the upper region. The signs of a_1 and b_1 changes alternatively like a wave in the region with large magnitude according to the spatial distribution of the time derivatives of p_3, and there occurs strong cancellation between contribution with opposite signs. But even after the strong cancellation, the upper part integral has dominant contribution to both a_1 at the time b and b_1 at the time α and β. These features are also seen in the smaller vortex ring with $R_0 = 5$.

Then let us consider the time dependence of the octapole mode amplitude $B_1(t)$. Equations (16) show that the function $b_1(\mathbf{y}, t)$ is approximately proportional to the time derivative of $a_1(\mathbf{y}, t)$ when the acoustic source is localized in a narrow region which does not move during the rapid change of the vorticity field. In the case of oblique collision, this condition is satisfied at around the time b as shown above. This explains the behaviour of B_1, which passes zero from positive to negative sign around the maximum of A_1.

The time evolution of the vorticity distribution shows that the vortexline reconnection begins during the time α and b. The contours *on* the symmetry plane (x_1, x_3) of the magnitude of ω_2-component which is perpendicular to the symmetry plane are illustrated in Fig.4(d). The large magnitude of ω_2-component means that there occurs vortexline reconnection. At the time α there exists almost no ω_2-component on the symmetry plane, but at the time b and β large amplitude of ω_2 exists in the region where vortex rings are in contact with each other. Comparing these contours with the spatial distribution of a_1 and b_1, we find that strong acoustic source exists in the region where vortexline reconnection occurs.

V. CONCLUDING REMARKS

A general formulation for the acoustic wave generated by a vortex motion is applied to the oblique collision of two vortex rings at right angles. The vortex motion in the collision process is simulated numerically by solving a viscous incompressible vorticity equation with a vorticity-potential method. The mode amplitudes of the far-field acoustic pressure are obtained by calculating the moment integrals of the vorticity distribution following the mathematical formula presented in Ref.[4]. Numerical simulations were carried out for two parameter sets of vortex rings which have the same vortex core but different ring radii. The slenderness ratio of a core radius to a ring radius is 0.2 for a smaller vortex ring and 0.1 for a lager vortex ring. It is shown that the slenderness ratio is one of the important factors to determine the acoustic emission from the vortex ring collision. Comparing the numerical mode amplitudes with the experimental ones, it is estimated that the slenderness ratio of the experimental vortex ring might be between 0.15 and 0.25. We have calculated the moments of the third and the fourth time derivatives of $p_3 = \frac{1}{2}(\mathbf{y} \times \omega)_3$ and confirmed which regions of the space contribute dominantly to the mode amplitudes A_1 and B_1 at the instance when the B_1 or A_1 mode amplitude has its peak value. Characteristic features of the local vortex motion relating to the quadrupole and the octapole acoustic emission are illustrated. It has been clearly shown that the region of strong acoustic source coincides with the region where vortexline reconnection occurs in the oblique collision of vortex rings.

References

1. T. Kambe, J. Sound Vib. **95**, 351 (1984).

2. T. Kambe, J. Fluid Mech. **173**, 643 (1986).

3. T. Kambe, *Theoretical and Applied Mechanics, 1992*, edited by S.R. Bodner, J. Singer, A. Solan and Z. Hashin (Elsevier Science, Amsterdam, 1993), pp. 239-255.

4. T. Kambe, T. Minota and M. Takaoka, Phys. Rev. E**48**, 1866 (1993).

5. L. Ting, J. Fluid Mech. **127**, 497 (1983).

6. K. Ishii, K. Kuwahara and C.H. Liu, Computers Fluids **22**, 589 (1993).

7. P.G. Saffman, Stud. Appl. Math. **49**, 371 (1970).

TABLES

TABLE I. Parameters and Time Scales.

	Case I	Case II	Simulation(Ref.[4])	Exp.(Ref.[4])
R_0	5.0	10.0	0.49	4.7mm
a_0	1.0	1.0	0.20	
$a_2(t=2)$	1.34	1.34	0.35	
Γ	62.8(20π)	62.8	2.99	
U_0	3.13	1.91	1.17	27.3×10^3 mm/s
ν	0.10	0.10	0.01	15mm^2/s
$Re = UR/\nu$	157	191	57.3	8550
$Re^* = \Gamma/\nu$	628	628	299	
$\lambda_0 = a_0/R_0[a_2/R_0]$	0.2[0.27]	0.1[0.13]	0.4[0.71]	
$T_1 = R_0/U_0$	1.60	5.23	0.42	0.172ms
$T_2 = a_0/U_0[a_2/U_0]$	0.319[0.427]	0.524[0.702]	0.17[0.3]	
$T_3 = a_0^2/\kappa[a_2^2/\kappa]$	0.10 [0.18]	0.10[0.18]	0.0841[0.251]	
$T_4 = a_0^2/(4\nu)[a_2^2/(4\nu)]$	2.5[4.5]	2.5[4.5]	1[3]	
$T_5 = R_0^2/(4\nu)$	62.5	250.0	6.0	0.368s
$U_1^* = U_0$	3.13	1.91	1.17	27.3×10^3 mm/s
$U_3^* = \kappa/a_0 \ [\kappa/a_2]$	10.0[5.56]	10.0[5.56]	2.38[1.36]	
$U_4^* = \nu/a_0$	0.1	0.1	0.05	

$$a(t) = \sqrt{4\nu(t + t_0)}, \quad U = \frac{\Gamma}{4\pi R}(\log(\frac{8R}{a}) - 0.558), \quad \kappa = \frac{\Gamma}{2\pi}$$
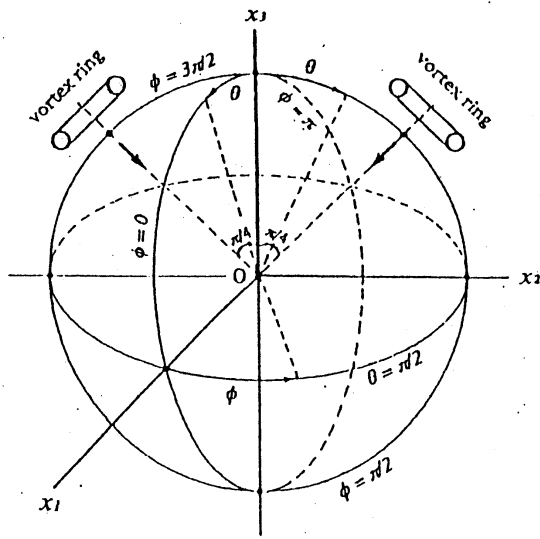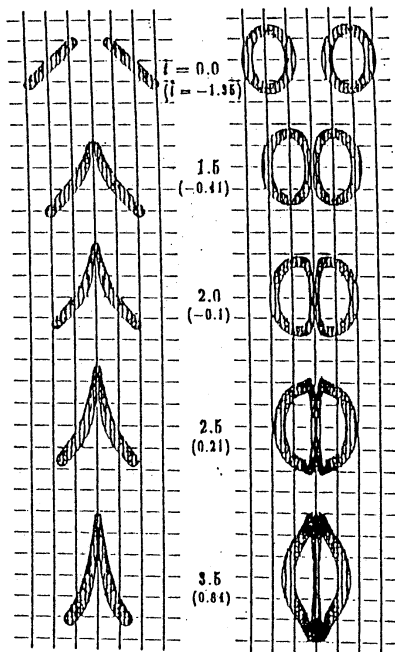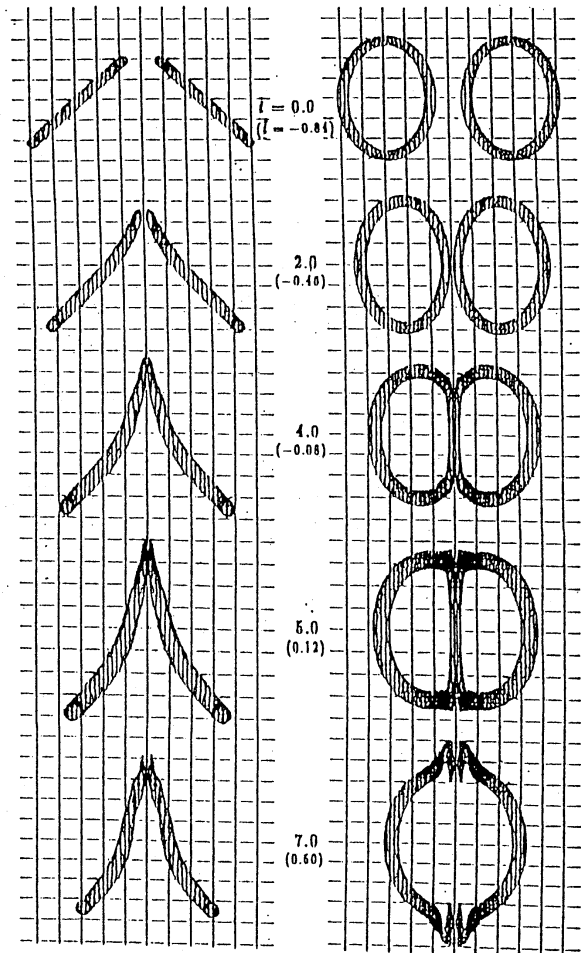
FIG. 1. Geometrical setup of the collision of two vortex rings and coordinate system.

(a) $R_0 = 5$

(b) $R_0 = 10$

FIG. 2. Side view (from the x_1 axis) and top view (from the x_3 axis) of the collision of two vortex rings at right angles for (a) $R_0 = 5$ and (b) $R_0 = 10$. The isovorticity surfaces of magnitude with 40% of the maximum at each instance are illustrated.
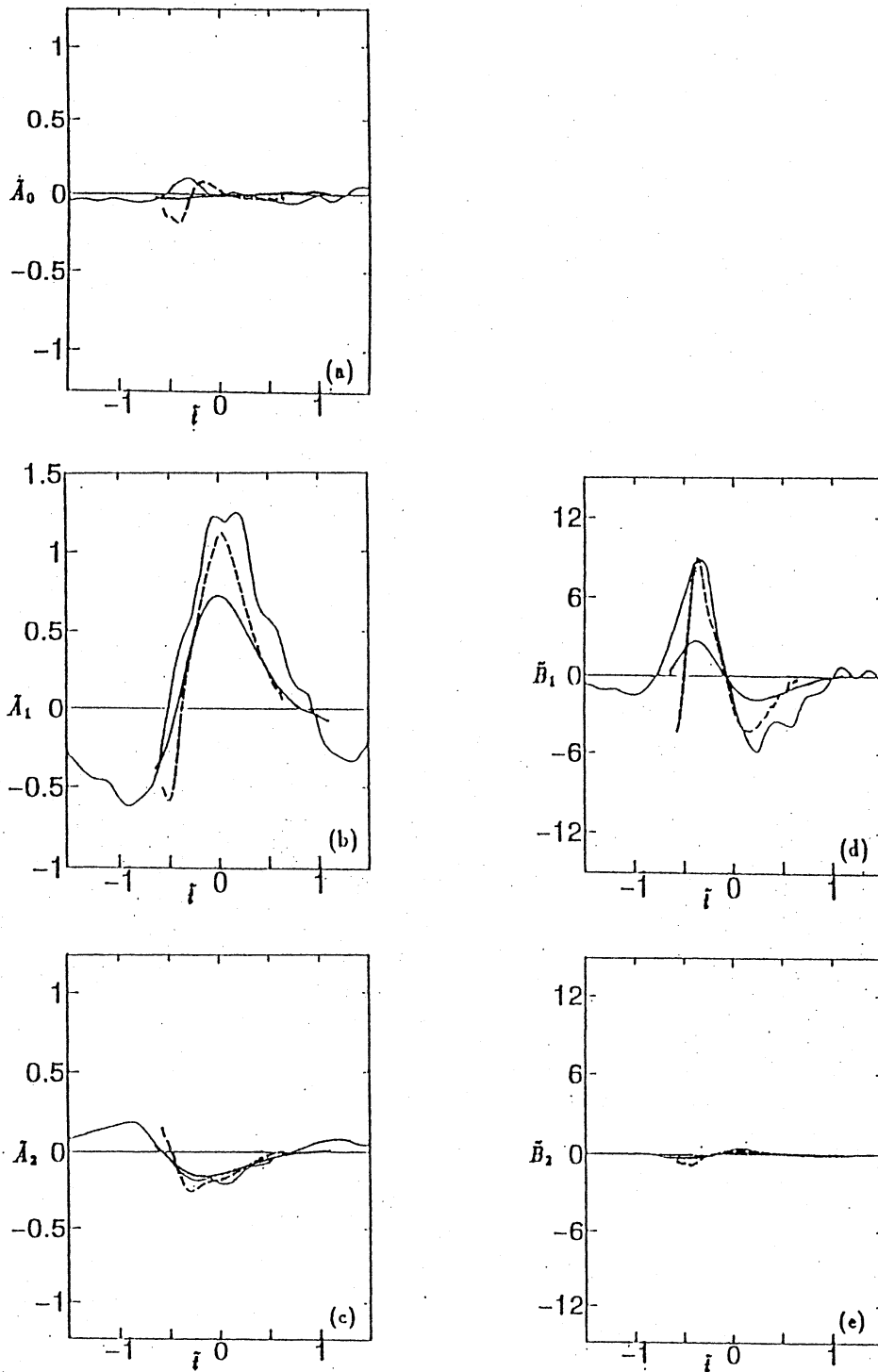
FIG. 3. Main mode amplitudes for (a) $\tilde{A}_0$, (b) $\tilde{A}_1$, (c) $\tilde{A}_2$, (d) $\tilde{B}_1$ and (e) $\tilde{B}_2$. Calculated amplitudes are drawn with thick solid lines for $R_0 = 5$ and with thick dashed lines for $R_0 = 10$. Observed amplitudes are shown with thin lines.
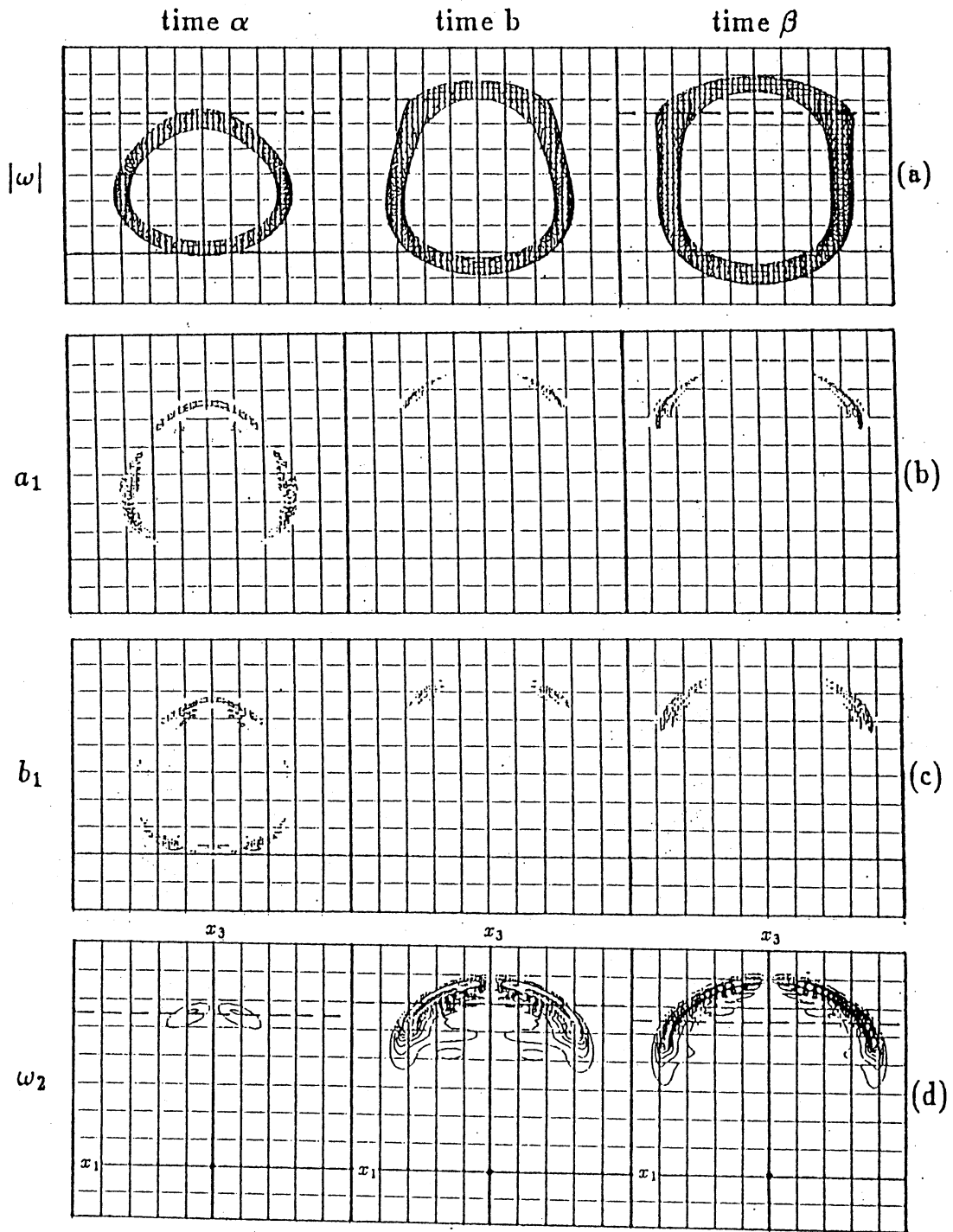
FIG. 4. Projective side views (from the x_2 axis) of (a) the isovorticity surface and the distribution of (b) a_1 and (c) b_1 for $R_0 = 10$ at the time α(positive peak of $\bar{B}_1$), b (positive peak of $\bar{A}_1$) and β(negative peak of $\bar{B}_1$). The distribution of (d) ω_2 on the (x_1, x_3) plane $(x_2 = 0)$.